J Mater Sci (2012) 47:668–676
DOI 10.1007/s10853-011-5837-5

Surface plasma resonance spectra of Au nanoparticles formed from dewetted thin films

Jia-Yu He · Jin-Xing Lu · Ning Dai · Da-Ming Zhu

Received: 28 April 2011 / Accepted: 29 July 2011 / Published online: 12 August 2011

Abstract We investigated surface plasma resonance (SPR) properties of gold (Au) nanoparticles formed by step-by-step thermal annealing of Au films deposited onto substrates. We found that the averaged sizes of the Au particles formed in the annealing process depend on the initial thicknesses of the films. Using the geometric parameters extracted from the images of Au particles, the optical transmission spectra measured can be completely described in terms of SPR in the particles. The results suggest that annealing of Au films can be a simple and effective approach for producing Au nanoparticles with desired optical transmission properties, and the approach can be easily integrated into thin film fabrication processes.

Introduction

Surface plasmons are collective oscillations of conducting electrons confined on metallic surfaces of nanoparticles or nanostructures on a surface [1]. Excitation of surface plasmons by an electrical field which is often associated with an incident light results in a buildup of charge polarization on the surface, which in turn acts as a restoring force to the charges, allowing for a resonance to occur at a particular frequency [1]. At the resonance, an incident light is strongly adsorbed or scattered [2, 3]; the frequency of surface plasmon resonance depends on the size and the shape of the particles as well as the nature of the dielectric medium surrounding the particles. Thus the resonance can be tuned through a wide range of wavelength [2, 3]. These characteristic properties of surface plasmon resonance offer great potential for the applications in different areas including the application of surface plasmon technique for optoelectronics device applications [4–6].

One of the applications is utilizing SPR in metallic nanoparticles for enhancing the efficiency of photovoltaic devices used in solar cells. Although solar cells have been widely considered as one of the most promising renewable energy devices [7, 8], the cost of photovoltaic modulus in solar cells is still a major barrier for the large scale adoption of the technique. One approach towards the cost reduction is using thin films to replace bulk silicon materials in building the photovoltaic modulus [9–11]. However, the efficiency of thin film solar cells is limited by relatively poor light absorption of the thin films in comparison to bulk materials-based solar cells. Also, because the thickness of thin films used in photovoltaic modulus in solar cells is typically on the order of micrometer, the standard methods used for increasing light absorption, such as the use of surface textures, cannot be applied to the thin film solar cell photovoltaic modulus [10, 11]. Thus, other approaches have to be adopted to mitigate the shortcoming of thin film photovoltaic modulus. One of the methods is to deposit a layer of metallic nanoparticles onto the surface of the modulus. When light strikes on the nanoparticle layer, surface plasmon resonances of the metallic particles enhance the light being scattered into the silicon film underneath and thus improve the light absorption of photovoltaic modulus [7–10]. By adjusting the size of the particles, the plasmon resonance peak of the nanoparticles can be tuned to match

J.-Y. He · J.-X. Lu · N. Dai · D.-M. Zhu
National Laboratory for Infrared Physics, Shanghai Institute of Technical Physics, Chinese Academy of Science, Shanghai 200083, China

D.-M. Zhu (✉)
Department of Physics, University of Missouri-Kansas City, Kansas City, MO 64110, USA
e-mail: zhud@umkc.edu

the spectral profile of the absorption power in the thin film of the solar cell [9, 11–17]. Indeed, significant increase of light absorption at specific wavelength has been demonstrated in solar cells by introducing metallic nanoparticles, although the overall improvement of energy conversion efficiency of the devices still needs to be tested [10, 14]. Besides enhancing the absorption rate in solar devices using metallic nanoparticles and other surface plasmonic structures, other approaches for increasing the absorption or recombination rate of photons in solar cells using novel active regions such as quantum wells or quantum dots with large optical matrix elements have also been recently demonstrated [9, 18–22].

Metallic nanoparticles can be synthesized using a number of different approaches [23–25]. But for large scale adoption and fabrication, the method has to be economically viable and compatible with the fabrication process of thin film photovoltaic modulus [10, 15]. The work done by Catchpole and Pillai showed that a thin metal layer deposited on a Si surface, followed by thermal annealing, can be transformed into a layer of metallic nanoparticles [10]. The method is simple and can be easily integrated into the thin film fabrication process, but questions regarding what the control parameter(s) can be used in this approach to control the particles' sizes and their optical properties need be addressed before the method can be adopted for the improvement of the efficiency of photovoltaic devices and in other applications.

The noble metal nanoparticles such as Ag, Au, Cu have distinct surface plasmon resonance effects [3]; nanoparticles made of these metals can be used in solar cell applications. For the purpose of demonstrating and studying the enhancement of the light absorption in noble metal nanoparticles due to surface plasmon resonance, using Au is a convenient choice because the system has been very well studied and the surface oxidation process is relatively easy to be controlled. In this work, we systematically investigated the changes in SPR spectra of Au particles fabricated by a step-by-step annealing process of as-deposited Au films with different thickness. We used scanning electron microscopy images to characterize the geometric parameters of the Au particles formed at each annealing step, and correlate the changes in the spectra with the geometric parameters. We have further calculated the extinction spectra using the experimentally determined geometric parameters and assume that Au particles have an oblate spheroid shape with a Gaussian size distribution. The measured and calculated spectra indicate that optical transmission properties of Au particles change systematically following step-by-step annealing, and these properties formed after repeated annealing are determined entirely by the film thickness of the as-deposited films.

Experimental details

Au was chosen as the depositing material in the study because prominent SPR behaviors have been observed in the system [3]. Three substances—silicon wafers, glasses, and fluorine-doped-tin-oxide (FTO) coated glasses were used as substrates for depositing Au films in this study. Silicon wafers are the common substrates used for fabricating solar cell photovoltaic modulus [8]. Glass and FTO coated glass substrates were used for the purpose of measuring transmission spectra of Au nanoparticles and for being able to simultaneously characterize the morphological configurations of nanoparticles using scanning electron microscope (SEM) consecutively after each thermal annealing step. We deposited Au on these three types of substrates and then annealed them in parallel. SEM images show that the changes in the films deposited on silicon wafers and glasses are almost identical as long as they have gone through the same annealing processes. The surface of FTO was slightly rougher than that of glass. The increased roughness of FTO causes the Au films deposited onto it a little bit easier to be broken up, but the differences appear to be not significant [26].

Before the use, the glass, the silicon wafers, and the FTO substrates were first cleaned using acetone to remove any organic contaminants. After that, the substrates were further cleaned in alcohol and deionized water, and were then dried using blown dry nitrogen gas. An array of the cleaned substrates was placed in a sputtering coater (BAL-TEC SCD 500) to start the deposition of the films [27]. The deposition chamber was evacuated to a base pressure of better than 10^{-4} m torr before the deposition process was started. In the sputtering process, a high voltage was applied to the Au target; the working pressure was set to be about 10^{-4} torr and working current be 20 mA by adjusting the argon flow density and current intensity. The sputtering speed was controlled at about 0.07 nm/s.

The deposition was stopped when the film thickness reached the target value. The films were examined using atomic force microscope (AFM) and scanning electron microscope (SEM) immediately following the fabrication; the surfaces of the films appear to be uniform and smooth. The as-deposited films were then annealed for about 1 h at an elevated temperature in a furnace; the heating rate during the annealing was controlled at about 20 °C/min. SEM imaging was then performed on the films deposited onto the silicon wafer and FTO glass substrates. Optical transmission spectra were then measured on the films deposited on glass and FTO substrates using an UV–Visible Spectrometer (Perkin Elmer Lambda 800/900 UV/Vis) and a Fourier transform infrared spectroscope (BRUKER Optics VERTEX 80 V). Optical transmission spectra of bare glass and FTO substrates were also

measured and used as baselines for subtracting off from the spectra measured on Au film deposited onto these substrates. The annealing and characterization procedures were repeated until the Au nanoparticles appear to reach the final equilibrium sizes and shapes and show no obvious changes.

Results and discussion

Morphological characteristics of the Au particles

The mechanism involved in producing Au nanoparticles by thermal annealing of an as-deposited Au film is the dewetting properties of Au on the substrate surfaces used, as being well demonstrated in the previous work [28–33]. The mechanism of break-up of the Au films regarding grain boundary grooves at the free surface versus voids at the interface have been addressed in detail by several well-known research groups [34–36]. The kinetics of dewetting in solid state thin films have been recently drawn considerable interests due to its fundamental importance in thin films fabrications and crystal growth [37–40]. A thin and continuous Au film deposited on a nonwetting substrate becomes discontinuous when the film is subjected to thermal annealing which increase the mobility of Au atoms in the film [28–33, 41]. If the annealing continues, holes start to develop and coalesce; the film gradually transforms into a layer of separated Au islands with random shapes and sizes on the substrate [29, 30]. A more ordered Au nanoparticle structure can be formed under a prolonged thermal annealing at a sufficiently high temperature, which provides sufficient thermal energy to the nanoparticles, allowing them to minimize their interfacial energy and reach their thermal equilibrium states [31, 34, 36, 42].

Figure 1a–c shows the changes of an Au film on a silicon substrate (the changes of the Au film on the glass substrate were found to be the same) with the as-deposited film thickness of 8 nm after being annealing at 270 °C for different time periods. The figures demonstrate that, indeed, as the annealing proceeds, the surface of the film breaks up, forming irregular and strip-like shaped clusters; the strip-like clusters gradually coalesce and form clusters. To characterize the morphological changes of the Au clusters due to annealing, we assume the shapes of the Au clusters are all approximately elliptical and averaged over all the particles in the SEM images to obtain an averaged aspect ratio. The images in Fig. 1 show that the aspect ratio decreases with the annealing; the shape of the clusters eventually becomes approximately spherical but randomly oriented after prolonged annealing.

Figure 1d plots the extinction (inverse transmission) spectra measured on the film on a glass substrate after being annealed in parallel with that on silicon wafer substrate shown in Fig. 1a–c. Each of the spectra shows a distinct extinction peak at about 600 nm; the peak remains at roughly the same position after being annealing repeatedly at this temperature. It has been demonstrated that for an Au nanoparticle with diameter of 100 nm, an extinction peak due to SPR in the particle would appear in the optical transmission spectrum at 580 nm wavelength [43]. The extinction peaks in the extinction spectra obtained in this work appear at the similar wavelength and have similar dependence with the size of the Au particles, and, thus, are

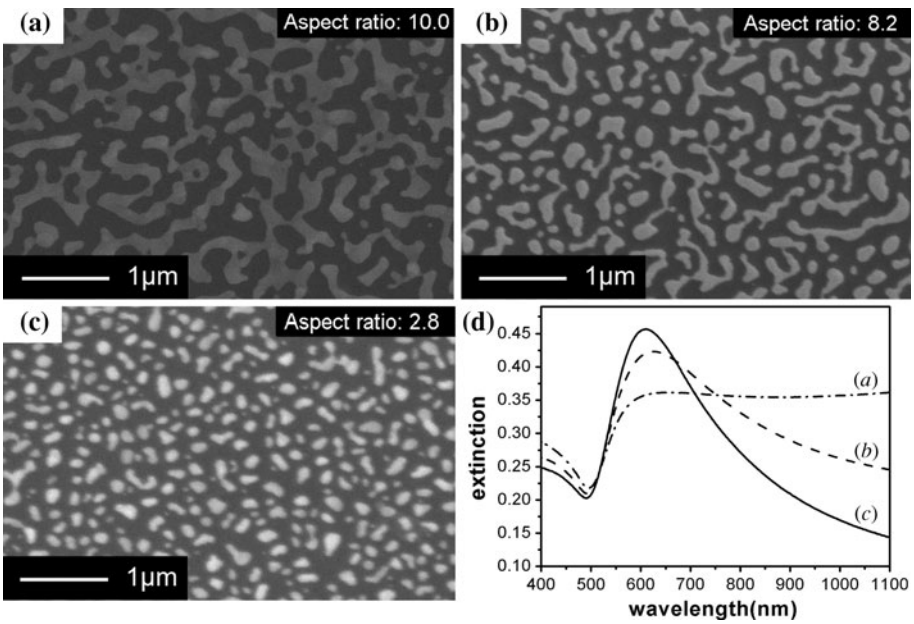

Fig. 1 Scanning electron microscopy images of surface morphology of a 8 nm thick Au film deposited on a glass substrate: **a** annealed at 270 °C for 1 h, **b** the same film as in **a** annealed accumulatively for 1.25 h at 270 °C, **c** the same film annealed at the same temperature accumulatively for 2.0 h. **d** Extinction (=log (1/transmission)) spectra measured on the film being annealed at stages shown in (*a*) (*dashed-dotted line*), (*b*) (*dashed line*), and (*c*) (*solid line*)

attributed to SPR in the Au clusters or nanoparticles formed from the Au films annealed at elevated temperatures. The morphology effects of SPR are not presented clearly in our results due to the fact that incident light was unpolarized and the particles are random oriented. The extinction spectra for clusters with larger aspect ratio have higher shoulders at the long wavelength limit. Such a behavior is reasonable since the clusters have large aspect ratio would absorb and/or scatter light of longer wavelength more strongly when the polarization is along the longer dimension in the clusters [44].

Figure 2a–c is SEM images of an Au film of 40 nm as-deposited thickness on a glass substrate after being annealed at 430 and 500 °C for different length of time. The morphological evolution of the particles is similar to that displayed in Fig. 1a–c, except that the Au clusters formed from this film are much larger. The extinction spectra (Fig. 2d) of these films shows a broad maximum peaked at about 2 μm. For films with strip-like morphology, the extinction peak is not distinct. But as the morphology becomes more cluster-like, the overall extinction peak rises and the maximum becomes more pronounced.

As mentioned above, the morphology of FTO was rougher than that of glass substrate. The roughness of FTO caused the films deposited onto the substrate not as continuous as that on glass substrate right after the depositions; the Au films became fractured more easily. Figure 3a–d shows the morphological changes of a Au film deposited on a FTO substrate with initial deposited thickness of 40 nm thick after being annealed at temperatures of 400 °C for different lengths of time. The extinction spectra of the film at different stages shown in the figures are displayed in Fig. 3e. The features revealed in the spectra are qualitatively the same as that in Figs. 1d and 2d.

The averaged size of the Au nanoparticles after prolonged annealing at elevated temperatures depends on the thickness of as-deposit film [40]. Figure 4a–f is the SEM images of the Au nanoparticles on glass substrates with the as-deposited film thickness varying from 6 to 20 nm, annealed at 600 °C for 1 h. The films were coated with a thin layer carbon conducting film right before the images were taken after all the annealing procedure and the transmission spectrum measurement were completed. The images show that the increased film thickness results in a corresponding increase of the averaged nanoparticle size. The averaged particle sizes are in the range from about 50 to about 500 nm as determined by analyzing the SEM images using the imaging processing software. It can be seen from the SEM images in Fig. 4a–d, while most of the particles have a circular shape after being annealed at the specified temperature, a small portion of the particles remained ellipsoid in their shape, as viewed along the substrate normal; the percentage of the ellipsoid shaped particles appears to increase with the thickness of the as-deposited film, as indicated in Fig. 4e, f.

Although the morphologies of the Au particles are affected by the annealing temperature and the annealing time, our results indicate that the averaged particle sizes, after prolonged annealing at about 600 °C, are determined by the thicknesses of the as-deposited films. It is possible to use the annealing temperature and the annealing time to control the particles' morphology, but it seems that using the thicknesses of as-deposited films as a parameter to control the final particles averaged size is a robust and easy approach in obtaining reproducible results.

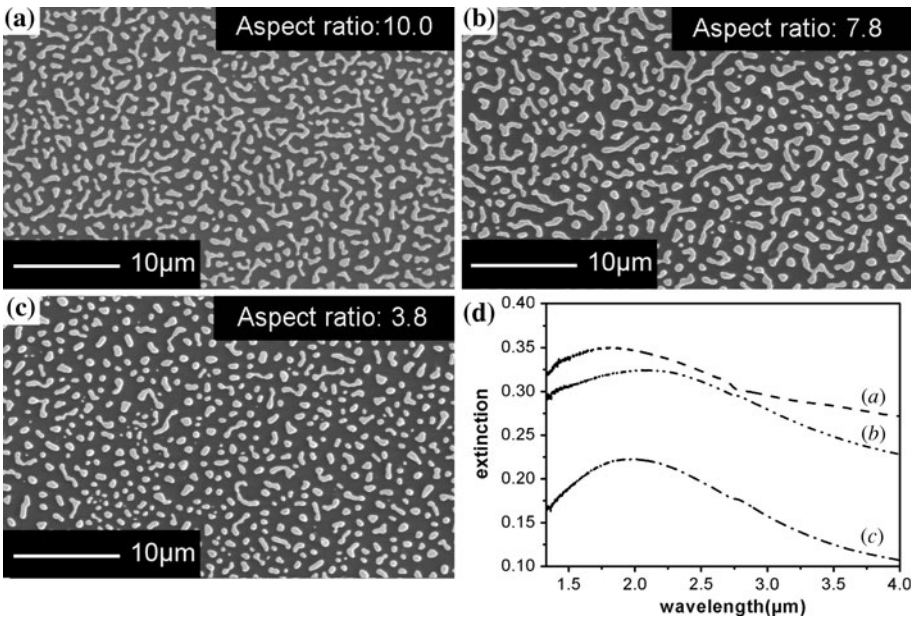

Fig. 2 Scanning electron microscopy images of surface morphology of a 40 nm Au film deposited on a glass substrate: **a** annealed at 430 °C for 1 h, **b** the same film as in **a** annealed at 430 °C for 1 h followed by annealing at 500 °C for 0.5 h, **c** the same film annealed at 430 °C for 1 h followed by annealing at 500 °C for 2 h. **d** Extinction (=log (1/transmission)) spectra measured on the film being annealed at stages shown in (*a*) (*dashed line*), (*b*) (*dashed-double dotted line*), and (*c*) (*dashed-dotted line*)

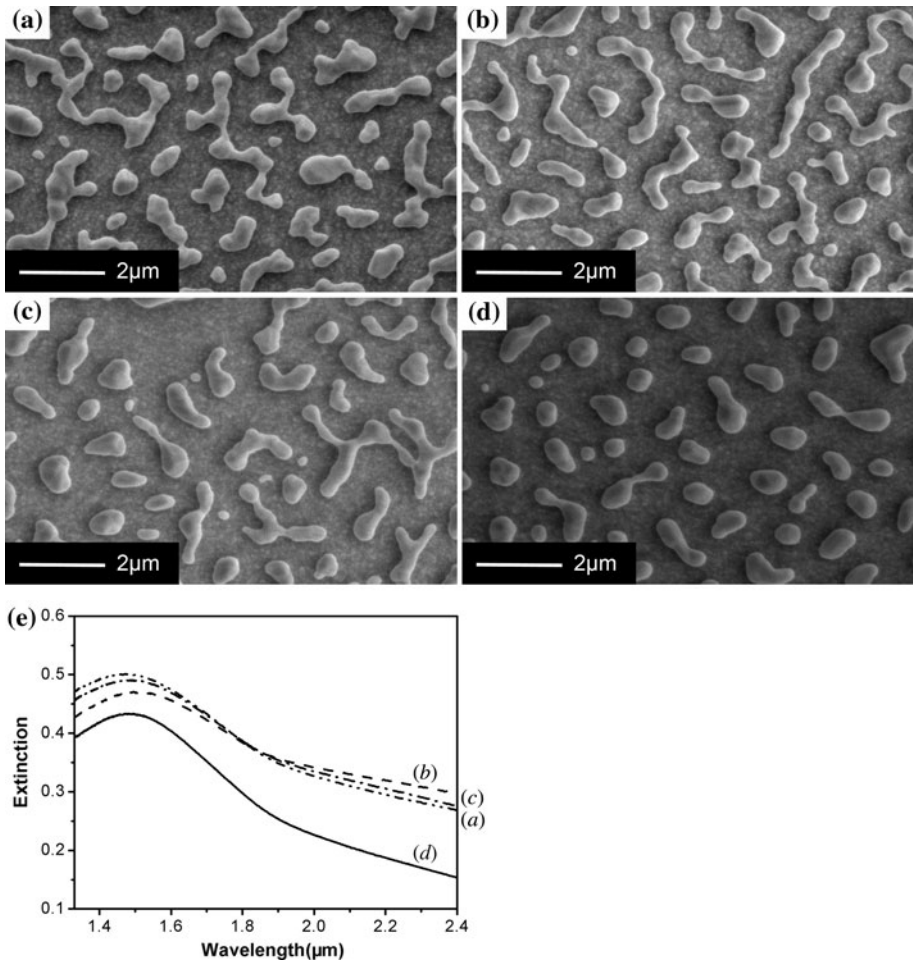

Fig. 3 Scanning electron microscopy images of surface morphology of a 40 nm thick Au film deposited on a FTO substrate: **a** annealed at 400 °C for 1 h, **b** continuously annealed at the same temperature for 0.25 h, **c** the same film annealed for another 0.25 h at the same temperature, total 1.5 h, and **d** the same film accumulatively annealed at 400 °C for 2 h. **e** Extinction (=log (1/transmission)) spectra measured on the film being annealed at stages shown in (*a*) (*dashed-double dotted line*), (*b*) (*dashed line*), (*c*) (*dashed-dotted line*), and (*d*) (*solid line*)

Optical SPR properties

The exact SPR behavior of a metal particle in a fixed dielectric environment depends on the size as well as the shape of the particle [3]. The shape effects have been elucidated clearly by comparing the cases of a metal sphere and that of spheroid [45]. One of the characteristics of SPR in spheroid shaped particles is that SPR depends strongly on the polarization of the field associated the incoming waves. If the field is directed along the ellipsoid axis, the resonance peak shifts to the red with increasing eccentricity of the ellipsoid [46, 47]. If the external field is directed perpendicular to the ellipsoid axis, SPR would shifts to the blue slightly with increasing eccentricity [46, 47]. In general, the resonance is dominated by the field in the direction along the longitudinal ellipsoid axis. In our study, the orientation of Au particles is completely random on the substrate. Thus, the effects of the elongated morphology of the particles spear out and cannot be seen in the spectra. But the general behavior of the SPR spectra of the particles after being annealed continuously, as shown in Figs. 1d, 2d, and 3e, is consistent with what have been described above: the magnitude of the extinction spectra at the longer wavelength decreases as the aspect ratio (or eccentricity) of the particles decreases after the step-by-step annealing.

Au particles become mostly in circular shape, viewing from the surface normal direction, after prolonged annealing at sufficiently high temperatures, as can be seen in Fig. 4a–f. To account for their SPR behaviors, we model these particles as oblate spheroids with longitudinal axis along the surface normal direction and transverse axis to be the radius of the particles determined from SEM images. We further assume that the variations in the diameter D of these particles can be described in terms of a Gaussian function [3]

$$f(D) = \frac{1}{\sigma\sqrt{2\pi}} \exp\left(-\frac{(D - D_0)^2}{2\sigma^2}\right) \quad (1)$$

where D_0 is the mean diameter of the disks, σ is the standard deviation of the diameter of the disks. Both D_0 and σ are determined from the analysis of the SEM images of the particles. We assume that the longitudinal axis of all the spheroids in the same sample have the same length and

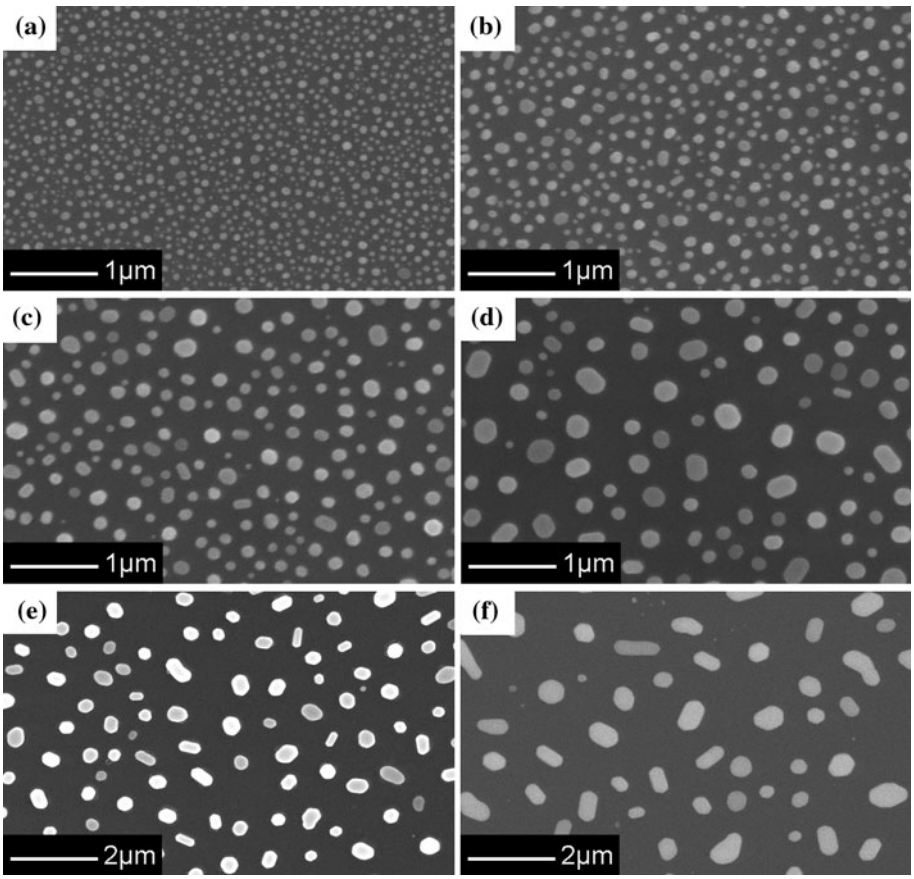

Fig. 4 SEM images of Au nanoparticles on glass substrates with increasing as-deposited film thickness. The as-deposited film thickness for samples **a–f** is 6, 7, 8, 9, 16, and 20 nm, respectively

determine this length by dividing the initial Au film thickness of each sample with the surface coverage which can also be extracted from the image processing procedure [48]. Table 1 lists these parameters for the six Au nanoparticle samples shown in Fig. 4a–f and the as-deposited film thickness; all of these parameters are determined from SEM images of the Au particles. Figure 5 shows the correlation between the mean diameter, the mean height, the standard deviation of the particles, and the as-deposited film thickness, respectively.

The dielectric constant of a particle can be size-dependent, if the radius of the particle is smaller than about 10 nm [3]. However, it has been demonstrated that, for Au nanoparticles with a diameter larger than 10 nm, their dielectric functions are very close to the bulk values and are size independent [3]. The size of nanoparticles we prepared in this study and used in this calculation is much larger than 10 nm, so we assume that dialectic function of the particle is the same as that bulk Au.

Table 1 Summary of geometric parameters of fabricated nanoparticles determined from SEM images

Film thickness (nm)	Mean diameter (nm)	Standard deviation in diameter (nm)	Surface coverage (%)	Mean height of spheroid (nm)
6	49.6	16.2	21.6	27.8
7	83.9	38.9	21.5	33.0
8	125.4	53.1	20.4	39.2
9	169.6	80.9	19.2	46.9
16	336.7	88.8	14.8	108.1
20	478.0	107.0	14.6	137.0

To perform the calculation and compare the results with the experimental spectra, the dipolar polarizability of each spheroid was calculated as a function of the geometrical parameters and dielectric response functions of Au and the surrounding medium. In the quasi-static limit (disk diameter $D \ll$ wavelength λ), the spheroid is treated as an individual dipole induced by an external field [2], which is parallel to the transverse axis of the spheroid. The dipolar polarizability of the spheroid is expressed as [2, 49–51]

$$\alpha(\omega) = \frac{\pi D^2 h}{6} \frac{\varepsilon_{\mathrm{Au}}(\omega) - \varepsilon_{\mathrm{m}}}{\varepsilon_{\mathrm{m}} + L[\varepsilon_{\mathrm{Au}}(\omega) - \varepsilon_{\mathrm{m}}]} \quad (2)$$

where L is a geometrical factor which is determined by the ratio of the longitudinal axis (h) and the transverse axis of the spheroid (D) of the particle, and $\varepsilon_{\mathrm{Au}}$ and ε_{m} are the dielectric functions of bulk Au and the embedding medium, respectively [52]. L can be approximately expressed as follows [2]:

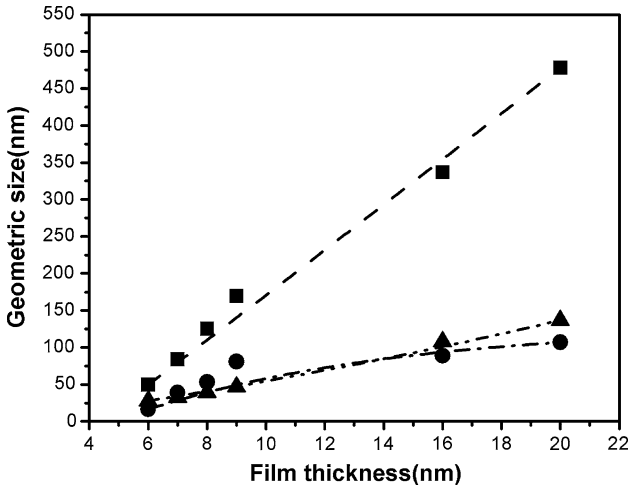

Fig. 5 The mean diameter (*square*), standard deviation (*circle*) in diameter, and the mean-height (*triangle*) of Au particles versus the as-deposited Au film thickness, determined from SEM images taken on different samples. The *lines* are the fits to the experimental data

$$L = \frac{g(e)}{2e^2}\left[\frac{\pi}{2} - \arctan g(e)\right] - \frac{g^2(e)}{2},$$
$$g(e) = \left(\frac{1-e^2}{e^2}\right)^{1/2},\ e^2 = 1 - \frac{h^2}{D^2}. \tag{3}$$

For the embedding medium, an effective refractive index ($n_{\text{eff}} = 1.26$) is used, which is the averaged value of air (1.00) and the glass substrate (1.52) [49, 50, 53, 54].

For larger disks ($D \sim \lambda$), finite wavelength effects are taken into account by adding a radiation damping and a dynamical depolarization term to the dipolar–polarizability function. The resulting modified expression for the dipolar–polarizability can then be written as [46, 49, 50, 53, 55, 56]:

$$\alpha'(D,\omega) = \alpha(\omega)\left[1 - i\frac{k^3}{6\pi}\alpha(\omega) - \frac{k^2}{2\pi D}\alpha(\omega)\right]^{-1} \tag{4}$$

where $k = 2\pi(\varepsilon_{\text{m}})^{1/2}/\lambda$ is the wave-vector of the incident light [57]. The k^3 term accounts for a radiation damping contribution, and the k^2 term accounts for dynamic depolarization. Based on the modified polarizability, the extinction efficiencies can be obtained [49, 50]:

$$Q_{\text{ext}}(D,\omega) = \left[\pi \cdot \left(\frac{D}{2}\right)^2\right]^{-1} \cdot k\text{Im}[\alpha'(\omega)] \tag{5}$$

The expression above can explain very well the results of monodisperse spheroids [46, 49–51, 57], but for the disperse spheroids here, the size distribution of particles must be considered in the calculation. We assume that the distribution of a spheroid's transverse diameter D can be described by $f(D)$ in Eq. 1. By weighting Q_{ext} using $f(D)$ and integrating over D, we calculated the extinction efficiency of an Au particle assembly. Figure 6a and b shows measured extinction spectra and calculated extinction efficiencies for Au nanoparticles specimen shown in Fig. 4a–d. The parameters used in the calculation are determined from SEM images of the specimen, and no free adjustable parameter is involved. The measured and calculated extinction spectra show the exactly the same behavior, both peak at about the same wavelength and have similar width. The measured extinction

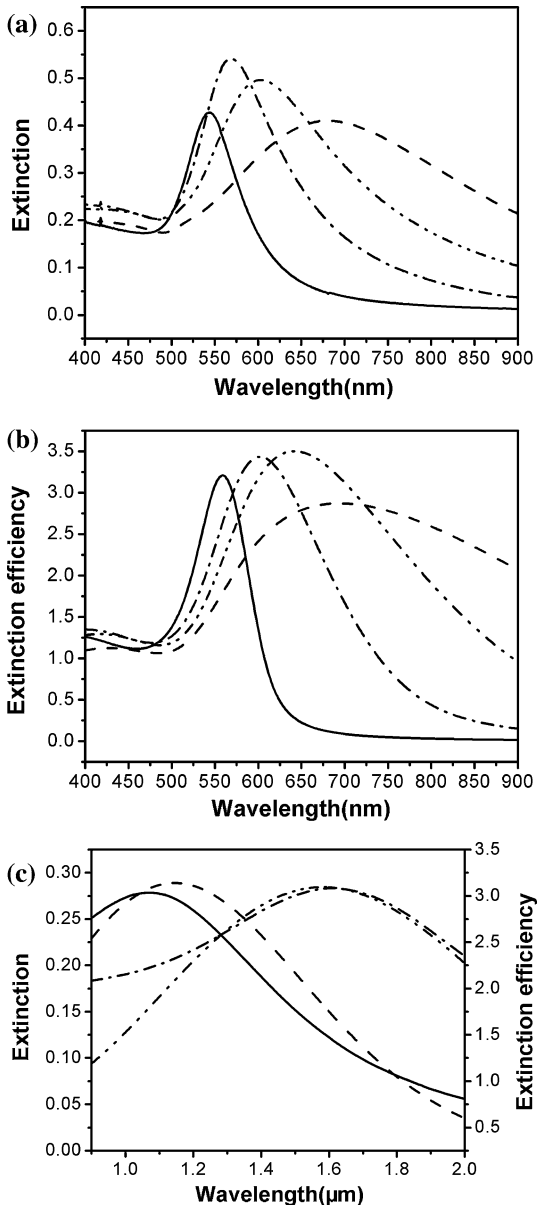

Fig. 6 **a** Measured extinction spectra (= log (1/transmission)) and **b** calculated extinction efficiency of Au spheroids with film thickness 6 nm (*solid line*), 7 nm (*dashed-dotted line*), 8 nm (*dashed-double dotted line*), and 9 nm (*dashed line*) using Mie theory and including the spheroids' size distribution. The distribution parameters are extracted from SEM images and are listed in Table 1. **c** Measured extinction spectra of Au spheroids with the film thickness 16 nm (*solid line*) and 20 nm (*dashed-dotted line*) and calculated extinction efficiency of Au spheroids with the film thickness 16 nm (*dashed line*) and 20 nm (*dashed-double dotted line*). The height (longitudinal axis) is assumed to be the same

spectra and calculated extinction efficiencies for larger Au nanoparticles displayed in Fig. 4e and f are shown in Fig. 6c. Here, the peak positions move to the infrared regime, but, still, the calculated extinction efficiencies display almost the same behavior as that of the measured extinction spectra. It should be noted that if the size distribution is not considered, the calculated spectra would have widths much narrower than that shown in the experimentally measured ones [49, 50, 53].

In Fig. 7, we plot the peak value and the full width at half maximum (FWHM) of the extinction spectra obtained on specimen with SEM images shown in Fig. 4 versus the as-deposited film thickness. Also plotted are the calculated peak positions and the FWHM of the extinction efficiencies using the parameters based on the line fits to the particle size distribution parameters extracted from SEM images. The peak positions and the widths and extinction peaks due to SPR in the extinction spectra are completely correlated with the thicknesses of the as-deposited films. The calculated extinction efficiencies show exactly the same correlation as that shown in the measured extinction spectra.

These results indicate that SPR spectra of Au nanoparticles produced by depositing Au films on silicon and glass substrates followed by subsequent annealing at temperatures in a range of 270–600 °C are controlled by the thickness of the as-deposited films. These results are not entirely surprising, since the Au particle formations are due to the morphological instability of the Au films in the dewetting processes. It has been demonstrated that the characteristic period of the surface modulation during the dewetting process scales linearly with the initial film thickness [58]. The surface modulation period determines the averaged size of the particles formed in the final stages

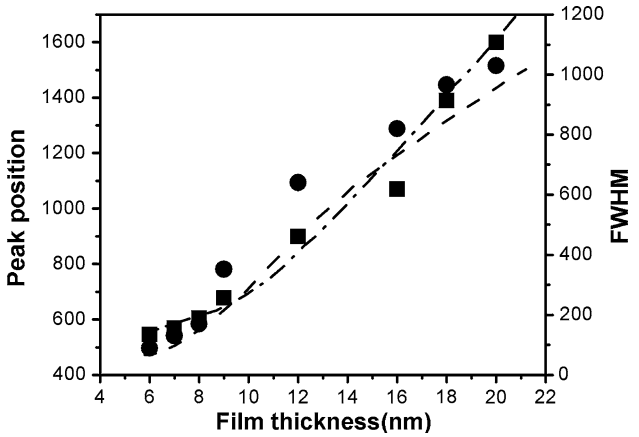

Fig. 7 The peak wavelength and the peak width (FWHM) of the SPR extinction spectra measured on Au nanoparticles with different as-deposited film thickness. *Square* peak wavelength and *circle* FWHM of the SPR peak. Also plotted are the peak wavelength and the FWHM extracted from the calculated spectra: (*dashed-dotted line*) peak wavelength and (*dashed line*) FWHM of the SPR peak

of the particle formation processes. Thus the optical properties of the finally formed Au nanoparticles can be tuned by the initial Au film thickness. This characteristic feature and the results presented above indicate that the method can be conveniently incorporated into the thin film fabrication processes for a wide variety of applications.

Conclusions

We have shown that by controlled annealing of Au films deposited on silicon, glass, and FTO substrates, Au particles with different morphology and sizes can be formed. The surface plasmon resonance excited on these particles show broad extinction peaks at wavelength from several hundred nanometers to a few micrometers. The peak values and the widths of extinction peaks are sensitive to the size and the size distribution of the particles, and can be easily tuned by varying the thickness of the as-deposited films.

Acknowledgements This project is fund by National Basic Research Program of China (Nos. 2010CB933700 and 2011CBA0900), 863 (No. 2009AA03Z412) and STCSM (No. 09ZR1436000), and by grant from Chinese Academy of Science in supporting an international collaborative research team.

References

1. Raether H (1988) Surface plasmons on smooth and rough surfaces and on gratings. Springer-Verlag, Berlin
2. Bohren CF (1983) Absorption and scattering of light by small particles. Wiley, New York
3. Kreibig U, Vollmer M (1995) Optical properties of metal clusters, springer series in material science, vol 25. Springer-Verlag, Berlin
4. Okamoto K, Niki I, Shvartser A, Narukawa Y, Mukai T, Scherer A (2004) Nat Mater 3:9
5. Okamoto K, Kawakami Y (2009) IEEE J Sel Top Quantum Electron 15:1199
6. Zhao HP, Zhang J, Liu GY, Tansub N (2011) Appl Phys Lett 98:151115
7. Jacobson MZ, Delucchi MA (2009) Sci Am 301(5):58
8. Green MA (2007) J Mater Sci Mater Electron 18:S15
9. Atwater HA, Polman A (2010) Nat Mater 9:205
10. Pillai S, Catchpole KR, Trupke T, Green MA (2007) J Appl Phys 101:093105
11. Catchpole KR, Polman A (2008) Opt Express 26:21793
12. Mertz J (2000) J Opt Soc Am B 17:1906
13. Derkacs D, Lim SH, Matheu P, Mar W, Yu ET (2006) Appl Phys Lett 89:093103
14. Beck FJ, Polman A, Catchpole KR (2009) J Appl Phys 105:114310
15. Catchpole KR, Polman A (2008) Appl Phys Lett 93:191113
16. Yeh DM, Huang CF, Chen CY, Lu YC, Yang CC (2008) Nanotechnology 19:345201
17. Henson J, Bhattacharyya A, Moustakas TD, Paiella R (2008) J Opt Soc Am B 25:8
18. Zhao HP, Liu GY, Tansu N (2010) Appl Phys Lett 97:131114
19. Zhang J, Zhao HP, Tansu N (2011) Appl Phys Lett 98:171111

20. Liao CT, Tsai MC, Liou BT, Yen SH, Kuo YK (2010) J Appl Phys 108:063107
21. Wu YR, Lin YY, Huang HH, Singh J (2009) J Appl Phys 105:013117
22. Liu G, Zhao H, Zhang J, Park JH, Mawst LJ, Tansu N (2011) Nanoscale Res Lett 6(1):342
23. Grigorenko AN, Geim AK, Gleeson HF, Zhang Y, Firsov AA, Khrushchev IY, Petrovic J (2005) Nature 438:335
24. Jensen TR, Malinsky MD, Haynes CL, Van Duyne RP (2000) J Phys Chem B 104:10549
25. Xiong Y, McLellan JM, Chen Yin JY, Li ZY, Xia Y (2005) J Am Chem Soc 127:17118
26. Lee KC, Lin SJ, Lin CH, Tsai CS, Lu YJ (2008) Surf Coat Technol 202:5339
27. Leica Microsystems GmbH, Ernst-Leitz-Strasse, 17-37 35578, Wetzlar, Germany
28. Srolovitz DJ, Safran SA (1986) J Appl Phys 60(1):247
29. Srolovitz DJ, Safran SA (1986) J Appl Phys 60(1):255
30. Shaffir E, Riess I, Kaplan WD (2009) Acta Mater 57(1):248
31. Baram M, Kaplan WD (2006) J Mater Sci 41(16):7775. doi: 10.1007/s10853-006-0897-7
32. Sadan H, Kaplan WD (2006) J Mater Sci 41(16):5371. doi: 10.1007/s10853-006-0407-y
33. Emundts A, Bonzel HP, Wynblatt P, Thurmer K, Reutt-Robey J, Williams ED (2001) Surf Sci 481(1–3):13
34. Chatain D, Wynblatt P, Rohrer GS (2005) Acta Mater 53(15):4057
35. Wang ZM, Wynblatt P (1998) Surf Sci 398(1–2):259
36. Sadan H, Kaplan WD (2006) J Mater Sci 41(16):5099. doi: 10.1007/s10853-006-0437-5
37. Ye J, Thompson CV (2011) Adv Mater 23(13):1567
38. Giermann AL, Thompson CV (2011) J Appl Phys 109(8):2011
39. Ye J, Thompson CV (2010) Phys Rev B 82(19):193408
40. Ye J, Thompson CV (2010) Acta Mater 59(2):582
41. Chatain D, Ghetta V, Wynblatt P (2004) Interface Sci 12(1):7
42. Gupta R, Dyer MJ, Weimer WA (2002) J Appl Phys 92:9
43. Kalyuzhny G, Vaskevich A, Schneeweiss MA, Rubinstein I (2002) Chem Eur J 8:17
44. Lu X, Rycenga M, Skrabalak SE, Wiley B, Xia Y (2009) Annu Rev Phys Chem 60:167
45. Grand J, Adam PM, Grimault AS, Vial A, Chapelle ML, Bijeon JL, Kostcheev S, Royer P (2006) Plasmonics 1:135
46. Kelly KL, Coronado E, Zhao LL, Schatz GC (2003) J Phys Chem B 107:3
47. Link S, EI-Sayed MA (1999) J Phys Chem B 103:8410
48. Temple TL, Mahanama GDK, Reehal HS, Bagnall DM (2009) Sol Energy Mater Sol Cells 93:1978
49. Langhammer C, Kasemo B, Zorić I (2007) J Chem Phys 126:194702
50. Langhammer C, Schwind M, Kasemo B, Zorić I (2008) Nano Lett 8:5
51. Landau LD, Lifshitz EM, Pitaevskii LP (1984) Electrodynamics of continuous media, 2nd edn. Pergamon, Oxford
52. Johnson PB, Christy RW (1972) Phys Rev B 6:4370
53. Langhammer C, Yuan Z, Zorić I, Kasemo B (2006) Nano Lett 6:4
54. Gotschy W, Vonmetz K, Leitner A, Aussenegg RF (1996) Appl Phys B 63(4):381
55. Wokaun A, Gordon JP, Liao PF (1982) Phys Rev Lett 48:957
56. Meier M, Wokaun A (1983) Opt Lett 8:581
57. Hanarp P, Kăll M, Sutherland DS (2003) J Phys Chem B 107:5768
58. Kwon SJ, Park JG (2006) Langmuir 22:3895